# The spectroscopic performance of the Swift X-ray telescope for gamma-ray burst afterglow studies

K. Mukerjee[a], J. P. Osborne[a], A. Wells[a], A. F. Abbey[a], A. P. Beardmore[a], A. D. Short[b], R. M. Ambrosi[a] and A. Moretti[c]

[a] University of Leicester, Leicester, UK
[b] ESTEC, Noordwijk, The Netherlands
[c] INAF Osservatorio Astronomico di Brera, Italy

## ABSTRACT

The *Swift* X-ray Telescope is a powerful instrument for measuring the X-ray spectral properties of GRB afterglows. The spectroscopic capabilities are obtained through the energy resolving properties of the X-ray CCD imager in the focal plane of the X-ray Telescope. A range of CCD operating modes allow GRB afterglows to be followed over 5 orders of brightness as the afterglow decays. The spectroscopic response in each mode has been determined as part of the XRT calibration programme and is being incorporated into the XRT instrument response matrices. These responses are being used to simulate GRB spectra as part of the pre-launch mission planning for *Swift*.

**Keywords:** X-ray telescope, X-ray CCD detector, Spectral Response, Swift, Charge-coupled device

## 1. INTRODUCTION

The X-ray telescope (XRT) is the instrument on board the *Swift* spacecraft designed to investigate gamma-ray burst afterglows in 0.2-10 keV energy band[1]. The instrument offers superior imaging capabilities and good energy resolution, along with high timing resolution. The intrinsic capabilities of this instrument together with the flexibility of the different data collection modes[2] makes it a superb tool for X-ray afterglow studies. The *Swift* XRT observations will be supplemented by simultaneous observations in the optical and UV performed by the UVOT. *Swift* is due for launch in early 2004.

The XRT uses nested grazing incidence Wolter-1 type X-ray optics[3] to focus incident X-rays onto the state-of-the-art CCD-22 based focal plane camera. The CCD-22 is a three phase frame transfer device, which utilises high resistivity silicon and an 'open' electrode structure, originally designed for the European Photon Imaging Camera on XMM-Newton[4]. The principal characteristics of the CCD-22 are summarised in Table 1. Other salient features of the CCD-22, along with its electrode structure, are described elsewhere[5].

The application of a CCD-22 as a focal plane detector for astronomy demands complete understanding of its response and its operational limitations. We are using a newly developed Monte-Carlo spectral response simulator to understand the features observed in the calibration data. In this paper we summarise the basic technique used for response development of the CCD and demonstrate its capabilities to resolve various spectral features as observed in the calibration data obtained during the laboratory calibration program carried out at the University of Leicester. The spectral response modeller is described briefly in Section 2, along with some of the important features incorporated in the code which allow us to generate the CCD quantum efficiency, resultant effective area and event pattern distribution. The results obtained from comparative studies of spectral response with the calibration data are presented in Section 3. Section 4 describes the development of the response matrices for three different data modes of the XRT. To demonstrate the capabilities of this instrument, we have simulated a spectrum based on GRB030329 using the XRT response matrix in Section 5.

**Table 1.** Characteristics of the *Swift* XRT CCD

| CCD Parameters | Characteristics |
|---|---|
| Pixel array | 600×600 |
| Pixel size | 40 $\mu$m × 40 $\mu$m |
| Imaging Area | 2.4 cm × 2.4 cm |
| Projected pixel size | 2.36 arc sec |
| Storage pixel array | 600 × 602 |
| Storage pixel size | 39 $\mu$m × 12 $\mu$m |
| Total active depth (Epitaxial layer) | 80 $\mu$m |
| Thickness of the Depletion region | 27 $\mu$m |
| Thickness of the Field Free region | 53 $\mu$m |
| Substrate thickness | 200 $\mu$m |
| Parallel charge transfer efficiency | $2.5\times10^{-6}$ per pixel |
| Serial charge transfer efficiency | $5\times10^{-6}$ per pixel |
| Electronics signal noise | 5 electrons |
| Data read out nodes | Left or Right or Simultaneous |

## 2. THE SPECTRAL RESPONSE MODEL

Response modelling software, based on a Monte-Carlo simulation technique, has been developed to enable a complete understanding of the performance of the CCD XRT focal plane detector. The response modeller considers incident photon transmission through the electrode structure of the CCD-22, the transmitted photons are then absorbed through photo-electric interaction at different depths in the device depending on the input energy and the linear absorption coefficient of the material. The simulation process includes the probability of secondary fluorescence emission, mainly silicon $K_\alpha$ which has a 4.4% yield. The emitted fluorescent photon is propagated in a random direction in space and a new trajectory is calculated, starting from the interaction position of the original photon*. The probability of fluorescent photons from other elements used in the construction of the CCD, such as oxygen and nitrogen, are very low and hence are not considered in the simulation.

The initial charge cloud, produced for each of the X-rays interacting in the CCD, undergoes spreading as it passes through the different active layers of the device. The spreading of the charge cloud (its shape, size and diffusion rate) depends on the physical properties of each layer. The spreading of charge and recombination losses have been appropriately accounted for in the modeller based upon the physical conditions in the different layers of the device. Those interactions occurring at the boundary of any two layers of the device have been carefully accounted for by introduction of a small offset to the appropriate parameters responsible for the real solution of the applied diffusion equations. Once the charge cloud reaches the buried channels, the total charge is distributed in multiple pixels according to the cloud size at the buried channel, which depends on the photon energy and its interaction depth. The modeller, therefore, incorporates pixel mapping and event reconstruction with accumulation of the charge due to the event. A single event threshold has been used for event reconstruction, set to 5 times the noise signal level.

Incident photons landing in the active region near the open electrode structure suffer from surface loss effects[5]. The charge loss depends on the energy and the attenuation depth of the photon. These losses have been modelled empirically by introducing loss parameters characterising charge loss as a function of depth and X-ray energy. The best values of these parameters are derived from fits to the calibration line profiles. The charge loss process due to charge transfer inefficiencies in the CCD has also been considered in the response generation. The effect

---

*Fluorescence events are included in the simulations, but are still to be included in the response matrices.
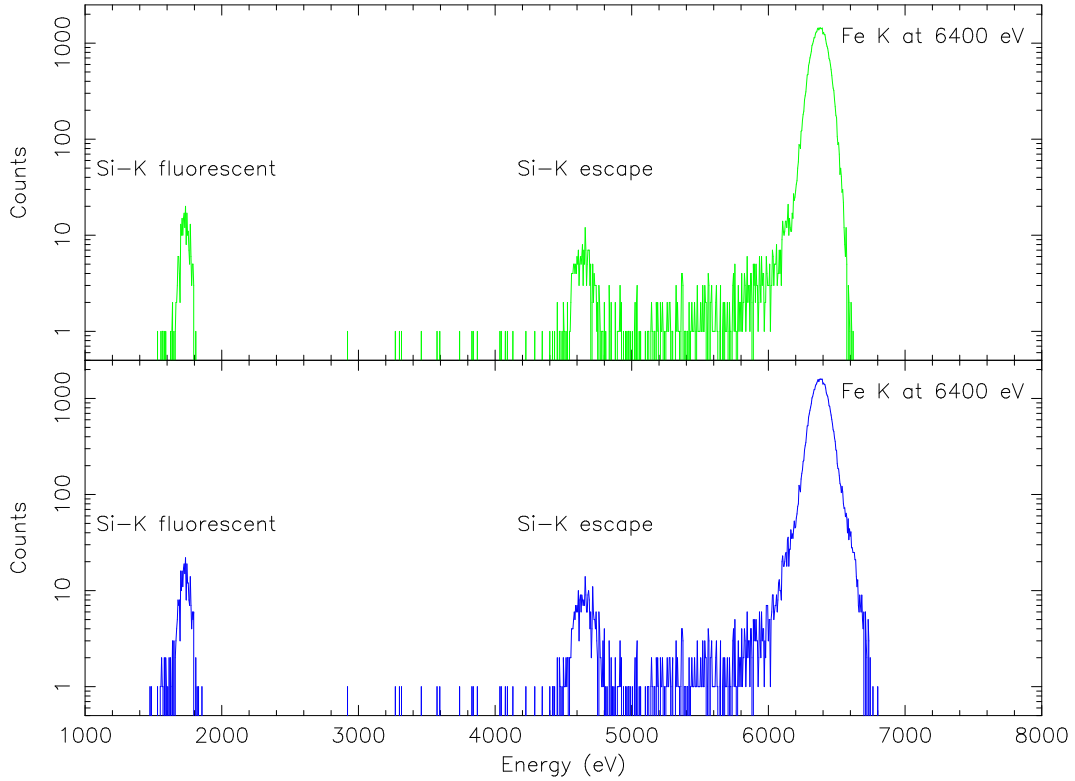
**Figure 1.** The simulated spectrum of Fe K$_\alpha$ (6.4 keV) obtained for isolated (top) and 1-2 pixel events (bottom) are shown.

of electronic noise is included prior to the pulse height reconstruction of individual events detected in the CCD. Neither charged particle background nor pile-up effects are modelled. The spectral response and other important characteristic features of the CCD, generated simultaneously by the response modeller, are discussed below.

## 2.1. A Simulated Spectrum

A simulated spectrum generated by the response modeller for isolated (single pixel) and 1-2 pixel events from iron K$_\alpha$ is shown in Figure 1. The total number of randomly distributed events considered in the simulation is $10^5$ at 6.4 keV. Three distinct peaks are observed in the the spectrum, corresponding to 6.4 keV as the input energy of the photons, the associated escape peak at 4.661 keV and the silicon fluorescent peak at 1.739 keV, as observed in laboratory data. There are only 4.4% of the events which are associated with fluorescent events in silicon. Depending on the absorption probability of the silicon fluorescent photon, it may escape from the original place of interaction and result in an escape peak. The silicon fluorescent photons, if absorbed in the active silicon may be detected as a separate event, giving rise to a separate distribution at 1.739 keV in the spectrum. The total integrated events in the above two spectra are consistent with the simulated quantum efficiency of the CCD at this energy, i.e. 42% for isolated events and 52% for 1-2 pixel events. Only 0.6% of the detected events contribute to fluorescent events as observed in the simulated spectrum. The extended lower energy redistribution of the main peak at 6.4 keV is due to a combination of surface loss and sub-threshold energy loss effects. The sub-threshold energy losses occur due to below-threshold pixels adjacent to detected events not being included in the charge reconstruction. Sub-threshold energy losses are the dominant effect for higher energy events, which undergo deeper interaction in the silicon and hence have a wider-spread charge cloud. At lower energies, the surface loss effects are dominant. The spectral redistribution on the lower side of the response is due to these charge loss effects. The 1-2 pixel event spectrum shows a wider spectral distribution compared to the single pixel
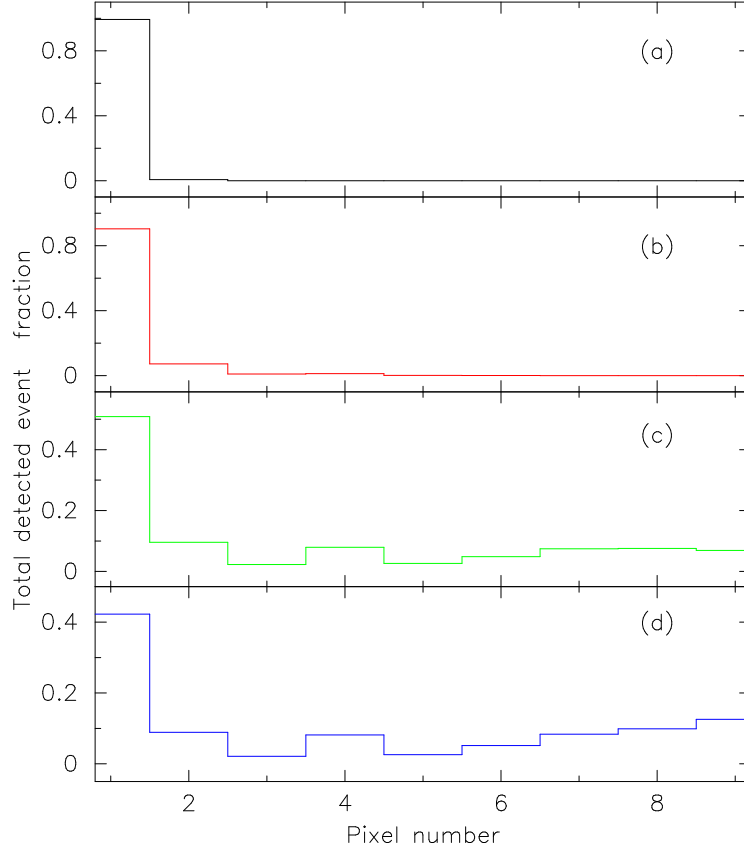
**Figure 2.** Event size distribution for 4 different energies are shown for (a) O K$_\alpha$ at 0.525 keV (b) Al K$_\alpha$ at 1.487 keV (c) Fe K$_\alpha$ at 6.403 keV and (d) Cu K$_\alpha$ at 8.048 keV.

events, due to the higher noise contribution following from the use of more pixels. The FWHM for iron K$_\alpha$ as simulated for isolated, 1-2 pixel, 1-4 pixel and 1-9 pixel events are 139, 142, 147 and 150 eV respectively.

## 2.2. The Event Size Distribution

The event size distribution as a function of event energy is generated in the simulations. The charge cloud produced by an X-ray photon within the active volume of the CCD drifts within the depletion region to the potential well minimum of a given pixel, resulting in a detected X-ray event. Due to the diffusion processes, the charge cloud attains a finite size, which can result in detection of an event with more than one pixel above threshold. All the X-ray events may therefore be classified depending on the event spread size in pixels and can be assigned an event grade or pattern. For example, if all the charge of an event is contained within a single pixel then it is identified as single pixel event, whereas, if the charge is distributed in 2 or more pixels, a specific grade or pattern is allocated to the event following the practise of the ASCA SIS or the EPIC MOS.

The event size distributions as predicted by the model at 4 different energies are shown in Figure 2. The pattern distribution clearly shows the dependence on the input photon energy. At the lowest energy considered here (0.525 keV) 96% of the detected events have a charge cloud confined to a single pixel, with no event spreading beyond two pixels. As the input energy increases, the event size becomes larger and progressively increasing contributions of charge in adjacent pixels are observed. At the highest energy considered here (8.048 keV) only 42% of the detected events are confined to a single pixel, whereas 2-pixel, 3-pixel and 4-pixel events account for 9%, 2% and 8% respectively. The rest of the events are distributed in larger events due to deeper interaction in the silicon.
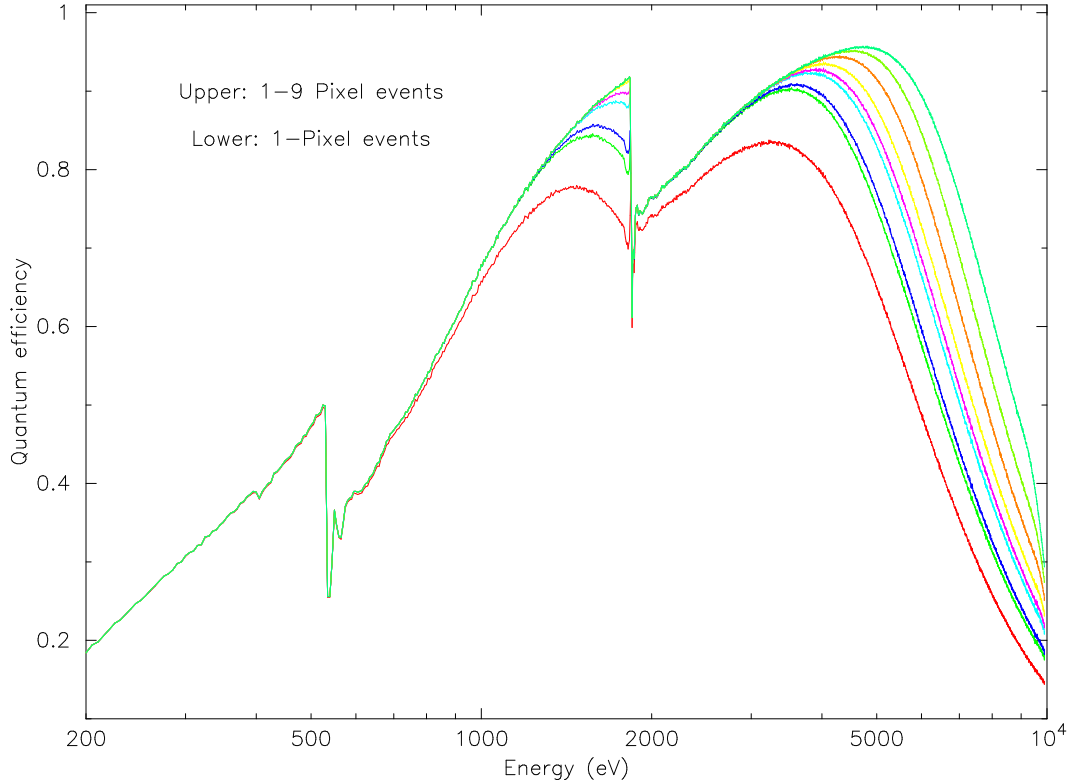
**Figure 3.** Quantum efficiency of CCD22 calculated for different events starting from 1-pixel events to 1-9 pixel events in the energy band 0.2-10 keV.

## 2.3. The Quantum Efficiency of the CCD

The electrode structure of a CCD-22 was specially designed to achieve a high quantum efficiency at lower energies by thinning and enlarging the polysilicon gates and leaving 40% of the pixel area open across the central electrode finger[4]. However, this design is susceptible to surface charge losses and traps. X-ray absorption in the dead layer overlying the depletion region determines the low energy X-ray response while the high energy response is limited by achievable depletion layer thickness.

Considering the electrode structure, and randomising the events on the surface of the CCD, the energy transmission through the electrodes is modelled to estimate the CCD quantum efficiency for the different sized events in the 0.2-10 keV energy band. The CCD quantum efficiency plots are shown in Figure 3. The absorption edges corresponding to oxygen and silicon are prominent. It is obvious that the quantum efficiency progressively increases from 0.2 keV to 1 keV, except at the oxygen K absorption edge, and is the same for all pixel events as at these energies only single pixel events are created. The CCD quantum efficiency above 1 keV up to 10 keV depends on the event size. Higher quantum efficiency is achieved by collecting charge from higher pixel event types. Selection of events of given sizes during data analysis will have an obvious impact on the overall effective area of the XRT.

## 2.4. The X-ray Telescope Effective Area

The XRT effective area is the product of the X-ray mirror effective area, the quantum efficiency of the CCD and the X-ray transmission of the optical filter. By considering these factors, the response modeller can calculate the XRT effective area as a function of energy. Figure 4 shows effective area plotted against energy for the different event sizes.
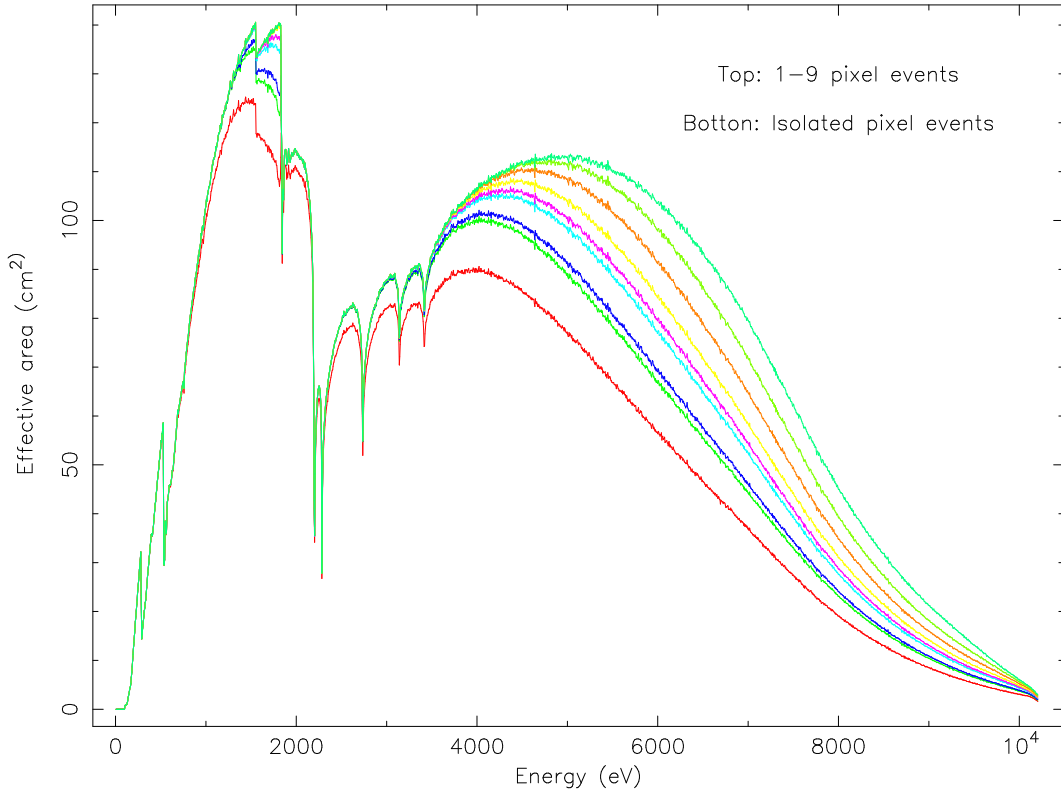
**Figure 4.** XRT effective area curves are plotted with energy for single pixel events (bottom) to summed 1-9 pixel events (top) as calculated during the simulation covering energy range from 0.1 to 10 keV.

If we consider 1-9 pixel events, the effective area is 40 to 50% higher with respect to single pixel events, while it is 15 to 20% higher with respect to 1-4 pixel events. In data analysis, inclusion of larger events results in higher effective area compared to just using the smaller events, however the spectral response broadens when larger events are used. Charged particles and piled-up X-rays also produce large events, possibly reducing their utility for scientific data analysis. Depending on the needs of the analysis, users will be able to make an appropriate event selection to optimise effective area, energy resolution and background.

## 3. COMPARISON OF MODEL AND DATA

A spectrum simulated for aluminium K$\alpha$ at 1.487 keV has been compared with the laboratory calibration data at same energy, obtained in the University of Leicester CCD testing facility. The laboratory calibration data includes background contributions such as bremsstrahlung and lines produced in the test facility. To extract the aluminium K$\alpha$ source spectrum from the laboratory data, the background was modelled with a 1 keV bremsstrahlung continuum, with contributions from various lines produced from the test facility. These are aluminium K$\beta$ at 1.557 keV, with an intensity normalised to 1% of the K$\alpha$ flux, and line emission at 2.013 keV to account for phosphorus K$\alpha$ in the target material. The background-subtracted spectrum was then normalised and re-binned as in the simulated spectrum for direct comparison. The two spectra are shown in Figure 5. The model:data ratio is shown below for direct comparison. The spectral comparison over the entire range of Figure 5 shows a very good match, although the spectral redistribution below 1 keV suffers from poor statistics in the simulated spectrum. The dynamic range of this well fit spectrum is almost 4 orders of magnitude and hence residual response calibration uncertainties will be below 0.1%.
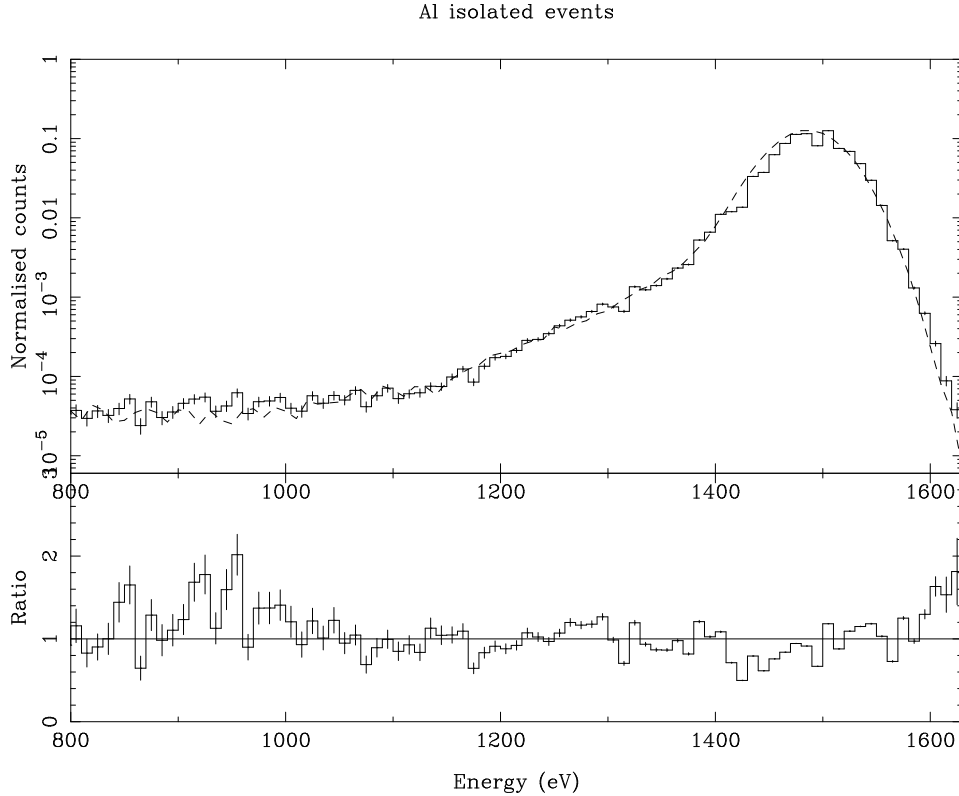
Al isolated events



**Figure 5.** Spectral data from laboratory calibration (dashed line) and simulated spectrum (solid line) for Aluminium $K_\alpha$ line at 1.487 keV is shown for comparison. Error bars show the statistical precision of the simulation.

## 4. RESPONSE MATRICES FOR THE XRT SPECTRAL MODES

The XRT is designed for completely automated operation, switching between different modes depending on the intensity of the target observed. During a typical GRB observation campaign the flux will decrease by 3 or more orders of magnitude. The XRT data modes are designed to avoid detector saturation at the early stages of the observation, while extracting as much information as possible at all stages. There are 4 data modes for XRT: Imaging, Photodiode, Windowed Timing and Photon Counting. The details of these modes and their capabilities for imaging, timing and spectroscopic studies are described in detail elsewhere[2]. Spectroscopic studies of GRBs will be made in the Photodiode, Windowed Timing and Photon Counting modes. Response matrices are needed for each mode.

In the non-imaging Photodiode and Windowed Timing modes the XRT only provides one-dimensional event patterns, and it is necessary to establish the relationship between event patterns in the different modes because the response width may be a function of the number of pixels sampled (due to their noise contributions).

The size of this effect depends upon the event size distribution actually observed. To understand the event pattern distribution in a CCD-22, we have analysed archival data from the XMM EPIC MOS obtained from observations of astrophysical sources. Three sources were carefully chosen such that all these sources have a thermal and a power law component in their spectrum and cover energy range 0.1-10 keV. The X-ray sources selected were the low mass X-ray binary EXO 0748-677, the supernova remnant Cassiopeia-A and the black hole candidate LMC-X3. The spectral nature of these candidates resemble GRB afterglow spectra to some extent, therefore studies of the event pattern distribution from these sources provides clues as to what to expect from a GRB. This study suggests that most of the X-rays from a GRB are expected to give rise to 1-2 pixel events (98%) while rest of the X-ray events (2%) cause 3 and 4-pixel events. The event pattern distribution, however,
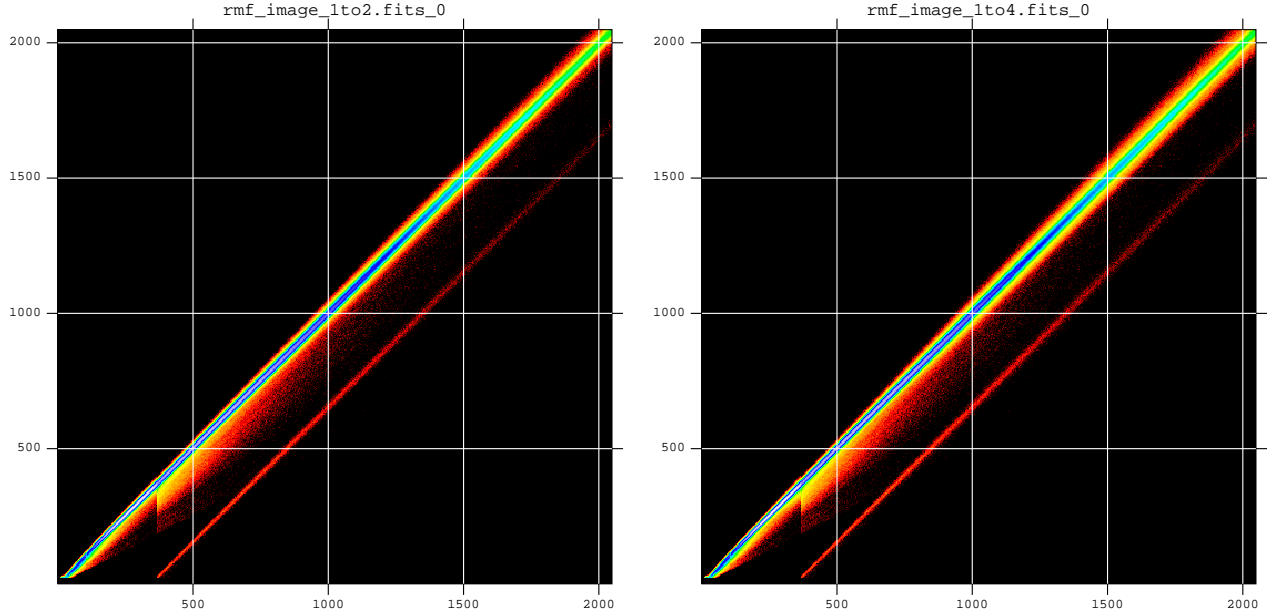
**Figure 6.** The CCD response for 1-2 pixel events (left) and 1-4 pixel events (right) are shown with the same linear scaling. The x-axis is the input photon energy, the y-axis the response. Both axes cover 0-10.24 keV.

depends on the degree of pile-up and on the contribution of the charged particle background in the data, both of which cause large-sized events.

## 4.1. Photon Counting Mode

Photon Counting mode is the most appropriate mode of the XRT for spectroscopic and imaging studies when the observed source flux is below 1 mCrab. We have developed response matrices for single pixel events, 1-2 pixel and 1-4 pixel events in this mode. Each of these responses offers specific advantages and their application depends on scientific needs of the data analysis. Figure 6 shows the response matrix developed for the XRT in Photon Counting mode for 1-2 and 1-4 pixel events.

The response matrices generated show a number of distinct features. The main spectral peak is represented by the main diagonal locus in Figure 6. The smear to the lower side of main peak is due to surface charge loss effects which increase to lower input energies. At higher energies surface loss effects are smaller, but energy redistribution occurs due to sub-threshold charge loss. The escape peak tracks the main peak for input photon energies above the silicon absorption edge at 1.839 keV. Above this edge there is a sharp reduction in the transmission of silicon so more X-rays interact near the surface of the device, populating the low energy side of the response. Thus the smear below the main peak reappears at 1.839 keV and slowly fades into the main peak at higher energies, as photons interact deeper in the active silicon. Broader distributions are observed in the response for higher pixel events such as the 1-4 pixel response matrix, as well as a higher number of total events due to larger effective area achieved.

## 4.2. Windowed Timing and Photodiode Modes

The response of the XRT in these two modes depends mainly on the event pattern transformation from the intrinsic two-dimensional patterns of Photon Counting mode. For example, 1-2 pixel events in Windowed Timing mode are mainly events that would have been seen as 1-4 pixel events in Photon Counting mode, similarly 1-3 pixel events in Photodiode mode are mainly 1-4 pixel Photon Counting mode events. It is possible to recover most of the original event patterns from these one-dimensional patterns. Based on the event pattern translations in these two modes, one can create an idealized response in these modes by the equivalent response in Photon
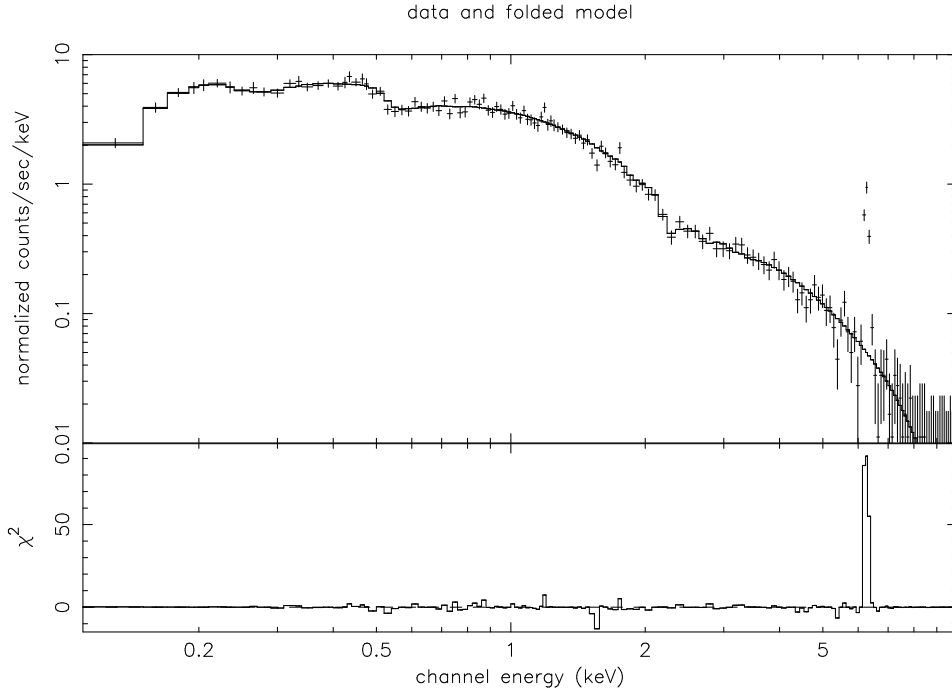
**Figure 7.** A simulated single pixel event XRT spectrum for Photon Counting mode. The model is the absorbed power law spectrum of GRB030329 observed around 5 hours. The data include an illustrative redshifted 6.4 keV iron line of 3 keV equivalent width (not seen in GRB030329). The detectability of the iron line is shown in the lower portion of the figure.

Counting mode. However, events selected as X-ray-like events in Windowed Timing and Photodiode mode may have a small contribution from background and pile-up. Spectral measurements conducted at Fe $K_\alpha$ shown that FWHM are consistent within measurement errors, for the spectral modes of the XRT. The measured FWHM for 1-4 pixel events in Photon Counting and its equivalent event pattern in Windowed Timing and Photodiode mode are respectively 156, 151 and 154 eV, consistent within the 7% measurement errors. Therefore, based on these concepts of event pattern translation, detector responses for the Windowed Timing and Photodiode modes have been developed for the purpose of data simulation. Mode dependent gain, offset and electronic noise effects will be included in the model, following analysis of calibration data obtained in these modes.

## 5. A SPECTRAL SIMULATION BASED ON GRB030329

We have used the isolated pixel response matrix file for Photon Counting mode with the mirror effective area and filter transmission to simulate an XRT GRB afterglow spectrum. The afterglow of GRB030329 was observed by RXTE in the 2-10 keV band from 4 hours 51 minutes after the GRB[6]. The afterglow was exceptionally bright, due to its unusual proximity (z=0.1685)[7]. The RXTE spectrum was fit[6] with an absorbed power law of photon index = 2, with the absorption later shown to be[8] $\sim 2 \times 10^{20}$ cm$^{-2}$. We created a simulated XRT spectrum using the observed spectral parameters, and in addition we added a redshifted emission line due to iron with an equivalent width of 3 keV (as was seen in GRB970508 at a later stage[9], such a line was not seen in GRB030329).

The simulated XRT spectrum of the GRB for a 30 minutes exposure, containing $1.3 \times 10^4$ counts is shown in the Figure 7. The net 0.2-10 keV count rate was 7.3 counts s$^{-1}$. This corresponds to flux of 0.13 photon $(2.1 \times 10^{-10}$ ergs) cm$^{-2}$ s$^{-1}$. Figure 7 shows a clear detection of the iron line in this exposure. Other spectral features visible include CCD absorption edges due to oxygen, at 0.532 keV, and silicon, at 1.84 keV (see Figure 3), and the series of gold M absorption edges in the mirror between 2.2 and 3.4 keV (see Figure 4). The spectral

features observed in the simulated spectrum and its compatibility with spectral analysis tools provides further confidence on the capabilities of the modelled XRT response.

## 6. CONCLUSION

We have modelled the X-ray response and detection properties of the focal plane detector of the *Swift* XRT, and have simulated various measurable characteristics of the CCD detector. We have successfully reproduced the Al K spectrum to a high level of precision. The detector response developed based on Monte-Carlo simulations has been found suitable for generating astrophysical simulations and conducting spectroscopic analysis of data in three different spectral modes of the XRT. We have also demonstrated that there are only small differences in the spectral resolution of the XRT between the Photon Counting, Windowed Timing and Photodiode modes, these differences can be modelled for inclusion in the response matrices. Further work is in progress to refine the detector response in these modes based on detailed analysis of the remaining calibration data.

## ACKNOWLEDGMENTS

## REFERENCES

1. D. N. Burrows, J. E. Hill, J. A. Nousek, A. Wells, G. Chincarini et al. *The Swift X-ray Telescope*, Proc. SPIE, 5165, in press, 2004.
2. J. E. Hill, D. N. Burrows, J. A. Nousek et al. *The X-ray Telescope read out modes*, Proc. SPIE, 5165, in press, 2004.
3. O. Citterio, S. Campana, P. Conconi, M. Ghigo, F. Mazzoleni et al. *The Characteristics of flight model optics for the JET-X telescope on board the spectrum x-gamma satellite*, Proc. SPIE, 2805, p 56-, 1996.
4. A. D. Holland, M. J. L. Turner, A. F. Abbey, P. J. Pool, *MOS CCDs for the EPIC on XMM*, Proc. SPIE, 1546, p 205–220, 1996.
5. A. D. Short, R. M. Ambrosi, M. J. L. Turner,*Spectral re-distribution and surface loss effects in Swift XRT (XMM-Newton EPIC) MOS CCDs*, NIM A, 484, pp 211–224, 2002.
6. F. E. Marshall and J. H. Swank *RXTE detection of GRB 030329 afterglow*, GCN 1996, 2003.
7. J. Greiner, M. Peimbert, C. Estaban et al. *Redshift of GRB 030329*, GCN 2020, 2003.
8. A. Tiengo, S. Mereghetti, G. Ghisellini, E. Rossi et al. *The X-ray afterglow of GRB030329*, astro-ph/0305564, 2003.
9. L. Piro, E. Costa, M. Feroci, G. Stratta, F. Frontera et al. *Iron line signature in X-ray afterglows of GRB by BeppoSAX*, Astronomy and Astrophysics Supp. Ser., 138, 431–432, 1999.